J. Fluid Mech. (2002), *vol.* 455, *pp.* 175–193. © 2002 Cambridge University Press
DOI: 10.1017/S0022112001007340 Printed in the United Kingdom

The start-up vortex issuing from a semi-infinite flat plate

By PAOLO LUCHINI[1] AND RENATO TOGNACCINI[2]

[1]Dipartimento di Ingegneria Meccanica, Università di Salerno, Italy

[2]Dipartimento di Progettazione Aeronautica, Università di Napoli Federico II, Italy

(Received 19 September 2000 and in revised form 18 September 2001)

The subject of the present work is the start-up vortex issuing from a sharp trailing edge accelerated from rest in still air. A numerical simulation of the flow has been performed in the case of a semi-infinite flat plate by solving the Navier–Stokes equations in the ψ-ω formulation. The numerical algorithm is based on a fast multigrid implicit integration of the difference equations in an unstructured mesh that is dynamically built to minimize the computational costs. A local refinement of the mesh near the edge of the plate increases the accuracy of the simulation. The results show that the asymptotic stage of the vortex evolution is self-similar in the mean, but the appearance of instabilities produces a time-dependent flow which is not instantaneously self-similar.

1. Introduction

The idea that the initial evolution of the start-up vortex shed by a sharp edge might be described by a class of self-similar solutions of the Euler equations dates back to Prandtl, but the determination of such a motion proved non-trivial. In particular, it is still an open question if, during this self-similar stage, the roll-up vortex is characterized by a regular and smooth evolution or, on the contrary, the spiral structure is quickly destroyed owing to an instability of the flow. In 1931, Kaden introduced similarity variables for describing the roll-up of a semi-infinite plane vortex sheet (Saffman 1992 p. 147). During the 1950s, several authors presented approximate asymptotic solutions in which the spiral vortex generated behind a sharp edge was replaced by a single point vortex, an example of which is given by Rott (1956). Moore (1976) studied and verified the stability of a class of vortex sheets rolling-up, but could not verify the stability of the present problem as noted by Pullin (1978). In the same work, Pullin, for the first time, obtained regular and well-defined start-up vortex spirals from an accurate numerical solution of the Birkhoff–Rott equation (inviscid flow) written in similarity variables.

On the other hand, many inviscid numerical simulations of the spiral evolution reported irregular behaviours, but the authors could not determine whether the instabilities were a property of the physical problem or were connected with the numerical algorithm (Sarpkaya 1989). Krasny (1991) obtained a smooth roll-up of the vortex, in size and shape comparable with Pullin's solution, by applying a vortex blob method to the time-dependent incompressible Euler equations; however, he was not able to ascertain the stability of this class of flows, nor was this clarified by experiments that, performed by different authors, proposed different conclusions (Pierce 1961; Pullin & Perry 1980).

https://doi.org/10.1017/S0022112001007340 Published online by Cambridge University Press

Luchini (I European Fluid Mechanics Conference, Cambridge, 1991, EUROMECH 305 and ERCOFTAC Workshop 'Dynamics and Geometry of Vortical Structures', Cortona, Italy, 1993, both oral communications) suggested an irregular evolution of the start-up vortex from the very early stage of its formation. More recently, simulations by a blob method of the viscous start-up for a plate of finite length have been proposed by Koumoutsakos & Shiels (1996). On the basis of their results the authors concluded that the start-up case with constant acceleration was unstable and characterized by irregular behaviour while, in the impulsive case, a regular development of the spiral vortex could be recognized even in the self-similar stage. Wang, Liu & Childress (1999) made a similar simulation of the impulsive start-up of an ellipse, reporting an irregular development of the spiral vortex. Luchini & Tognaccini (1999) noted an agreement between the viscous and the inviscid start-up developments, with the inviscid simulation performed by a non-regularized blob method. However, to assess the initial stages of this physical phenomenon better, the need was felt for more accurate viscous numerical simulations of the self-similar birth of a start-up vortex issuing from a semi-infinite flat plate, computed by solving the Navier–Stokes equations in the streamfunction–vorticity formulation. This is the objective of the present paper.

The main difficulty in the definition of a proper numerical algorithm for the integration of these equations is in the truncation of the theoretically unbounded solution domain and in obtaining a fast integration scheme in order to produce sufficiently accurate unsteady solutions in a reasonable computation time.

As a first step toward these goals, the governing equations have been re-written in a suitable non-dimensionalization involving a length scale depending on time. In the new variables, the enlargement of the spiral with time is slower, thus allowing the introduction of a lower number of discretization points. Furthermore, the accuracy required to avoid numerical smearing of the computed solution led to the development of a new and particularly efficient integration algorithm. The scheme is implicit, second-order accurate in both time and space coordinates. The number of unknowns is minimized by adopting an adaptive, unstructured grid of square cells. Grid points are introduced only in the region of non-negligible vorticity and the streamfunction on the consequent time-dependent numerical boundary is computed by using the Green integral. The implicit formulation requires a large linear system to be solved at each time step; this task is performed by a multigrid technique properly adapted to the unstructured grid. An efficient restriction algorithm increases the smoothing factor to a value of 9, thus allowing convergence to be obtained at each time step in 4–5 multigrid cycles only. In order to eliminate oscillations of the solution near the edge of the plate owing to the locally large flow gradients, the multigrid integration scheme has been coupled with a local refinement of the mesh. In this way, the accuracy at the edge of the plate has been improved without the need to reduce the mesh size elsewhere.

Through this algorithm, simulations with different scales of length and mesh sizes have been made possible. Following the presentation of the physical problem and of the numerical algorithm, the results obtained will be discussed in detail and compared with the available experiments and numerical solutions.

2. The physical problem

Let us consider a body with a sharp trailing edge that is accelerated from rest in a fluid. While time increases, four main stages can be recognized during the evolution of the start-up spiral vortex issuing from the sharp trailing edge:

https://doi.org/10.1017/S0022112001007340 Published online by Cambridge University Press

(i) Rayleigh stage: the flow is potential everywhere except for a thin Rayleigh-type viscous layer with constant thickness around the body.

(ii) Viscous stage: the convective terms of the Navier–Stokes equations become comparable with the viscous terms and thus a vortex structure begins to appear.

(iii) Self-similar inviscid stage: convective terms become dominant, but the vortex is still small enough to be independent of geometry except for the local wedge angle.

(iv) Vortex expulsion: the initial recirculation bubble opens up and the vortex starts lagging behind the body.

In the present paper, we undertake the simulation of the first three stages by solving the two-dimensional incompressible Navier–Stokes equations in a Cartesian domain (x, y) around a semi-infinite flat plate ($y = 0$, $x < 0$) in a streamfunction $\psi(x, y, t)$, vorticity $\omega(x, y, t)$ formulation:

$$\nabla^2\psi = \omega, \quad \omega_t + \psi_y\omega_x - \psi_x\omega_y = \nu\nabla^2\omega, \tag{2.1}$$

where ν is the kinematic viscosity. The conditions to be imposed at the plate are

$$\psi_y(x, 0^{\pm}, t) = \psi(x, 0^{\pm}, t) = 0, \quad x < 0. \tag{2.2}$$

In the far field, the streamfunction approaches the limiting inviscid solution of the potential flow equations around an infinite wedge (see for instance Batchelor 1967 p. 410). In the case of a power-law variation of the far-field velocity with time, this condition can be expressed as:

$$r \to \infty : \psi \to \psi_\infty(r, \theta, t) = At^a r^m \cos(m\theta). \tag{2.3}$$

where (r, θ) are polar coordinates. The coefficient m is related to the wedge angle $\beta = \pi(2 - 1/m)$ and is equal to $\frac{1}{2}$ in the case of a flat plate. With the assumed time variation of the potential far-field velocity (power-law), a self-similar behaviour of the inviscid solution in stage (iii) is allowed.

The vortex quickly grows with time; therefore the adoption of a time-dependent reference system can make a significant improvement to the computational efficiency by limiting the growth with time of the number of grid cells necessary for an accurate description of the spiral. In inviscid similarity coordinates, the size of the spiral would remain constant once the inviscid self-similar stage is reached; however, these coordinates are not appropriate during the vortex formation (for $t \to 0$, the size of the spiral becomes infinite in similarity coordinates); on the contrary, a slight growth of the vortex size with the consequent increasing of the grid resolution would be useful for large time values. The initial stage of the vortex roll-up is characterized by the formation of a Rayleigh type flow around the plate. The thickness of the viscous layer R is then constant along the plate and depends on time according to the law $R = \sqrt{k\nu t}$. These considerations suggest the use of R for scaling the spatial coordinates. We use the following transformation:

$$\left.\begin{aligned} &x = \bar{x}R, \quad y = \bar{y}R, \\ &\psi = \nu\bar{\psi}, \quad \omega = \frac{\nu}{R^2}\bar{\omega}, \quad t = t_v\bar{t}^k, \quad \frac{1}{k} = a + \tfrac{1}{2}m, \end{aligned}\right\} \tag{2.4}$$

with t_v a reference time given by

$$t_v = \left(k^{-m/2}\nu^{1-(m/2)}\frac{1}{A}\right)^k. \tag{2.5}$$

https://doi.org/10.1017/S0022112001007340 Published online by Cambridge University Press

By inserting (2.4) into (2.1)–(2.3), we obtain:

$$\bar{\nabla}^2\bar{\psi} = \bar{\omega}, \quad \bar{t}\bar{\omega}_{\bar{t}} + [(\bar{\psi}_{\bar{y}} - \tfrac{1}{2}k\bar{x})\bar{\omega}]_{\bar{x}} + [(-\bar{\psi}_{\bar{x}} - \tfrac{1}{2}k\bar{y})\bar{\omega}]_{\bar{y}} = \bar{\nabla}^2\bar{\omega}, \tag{2.6}$$

with boundary conditions:

$$\left.\begin{aligned} &\bar{\psi}_{\bar{y}}(\bar{x}, 0^{\pm}, \bar{t}\,) = \bar{\psi}(\bar{x}, 0^{\pm}, \bar{t}\,) = 0, \quad \bar{x} < 0, \\ &\bar{r} \to \infty : \bar{\psi} \to \bar{\psi}_{\infty}(\bar{r}, \bar{\theta}, \bar{t}\,) = \bar{t}\bar{r}^m \cos(m\bar{\theta}). \end{aligned}\right\} \tag{2.7}$$

Finally, on introducing the new time variable $\tau = \ln \bar{t}$ and defining $u = \bar{\psi}_{\bar{y}} - \frac{1}{2}k\bar{x}$, $v = -\bar{\psi}_{\bar{x}} - \frac{1}{2}k\bar{y}$, the vorticity equation takes back the usual form of the convection–diffusion of a scalar variable:

$$\bar{\omega}_{\tau} + (u\bar{\omega})_{\bar{x}} + (v\bar{\omega})_{\bar{y}} = \bar{\nabla}^2\bar{\omega}. \tag{2.8}$$

After this scale transformation the only parameters left are m, related to the geometry and a (appearing through the constant k), related to the law of unsteady start-up. In fact, for $a = 0$, the outer velocity is independent of time and represents the case of impulsive acceleration of the plate to a constant speed. For $a = 1$, the outer velocity grows linearly with time, and acceleration is constant; $a = \infty$ represents an infinitely smooth (C_∞) exponential start-up.

The reference time t_v is associated with the time scale of the viscous stage in which viscous and inviscid terms are of the same order of magnitude. The comparison of the convective term with the diffusive terms provides:

$$\frac{u_{ref}\omega_{ref}}{R(t_v)} \approx \frac{\nu\omega_{ref}}{R^2(t_v)}, \tag{2.9}$$

where u_{ref} and ω_{ref} are the reference velocity and vorticity. If u_{ref} is obtained considering the far-field behaviour (2.3) ($u_{ref} = \psi_\infty[R(t_v), t_v]/R(t_v)$), its substitution into (2.9) produces (2.5).

A Reynolds number characterizing the start-up vortex was introduced by Pullin & Perry (1980) for the purpose of describing their experiments. They derived it from dimensional analysis assuming that the path of the vortex core depends, during the spiral evolution, on the inviscid similarity coordinates and on the viscosity. They obtained:

$$Re_S = \frac{A^{2/(2-m)}t^{2(1+a)/(2-m)-1}}{\nu}, \tag{2.10}$$

or, in terms of our non-dimensional time $\bar{t}$:

$$Re_S = \left(\frac{\bar{t}^2}{k^m}\right)^{1/(2-m)}. \tag{2.11}$$

In order to gain an appreciation of the time scales involved in a practical situation, we may consider the case of a flat-plate airfoil at incidence. The value of A is obtained from the leading term of the local power expansion of the inviscid potential flow near the trailing edge. For a flat-plate airfoil the streamfunction is expressed, in the neighbourhood of the trailing edge, by

$$\psi \approx V_\infty(t)\sqrt{r}\sin\alpha\sqrt{c}, \tag{2.12}$$

where V_∞ is the free-stream velocity, α the angle of attack and c the chord length. From comparison of this formula with equation (2.3) we obtain, for a power-law

https://doi.org/10.1017/S0022112001007340 Published online by Cambridge University Press

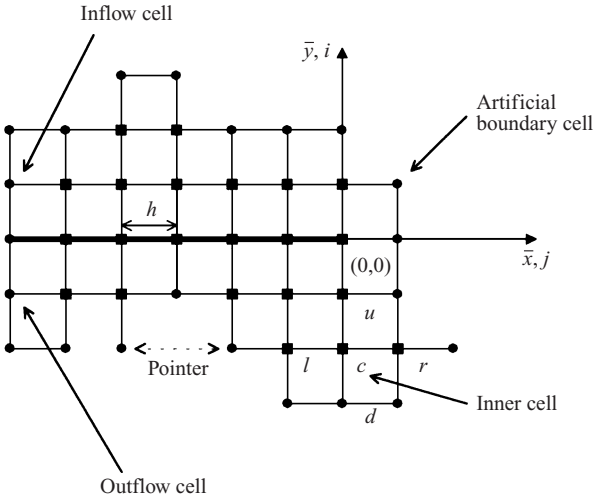


FIGURE 1. Scheme of the unstructured grid. Squares specify internal grid points, circles specify boundary grid points.

acceleration of the form $V_\infty = Bt^a$,

$$A = B \sin\alpha \sqrt{c}. \tag{2.13}$$

In the case of standard-atmosphere gas properties, $\alpha = 10^\circ$ and $c = 0.1\,\mathrm{m}$, we obtain for a step-velocity start-up with $V_\infty = 1\,\mathrm{m\,s^{-1}}$:

$$A = 0.055\,\mathrm{m^{3/2}\,s^{-1}}, \quad t_v = 2.7 \times 10^{-11}\,\mathrm{s}, \quad R(t_v) = 0.032\,\mu\mathrm{m}$$

while for a constant acceleration start-up of $9.8\,\mathrm{m\,s^{-2}}$:

$$A = 0.54\,\mathrm{m^{3/2}\,s^{-2}}, \quad t_v = 1.7 \times 10^{-3}\,\mathrm{s}, \quad R(t_v) = 0.12\,\mathrm{mm}.$$

It can be noted that the time scale characterizing the vortex formation is extremely small in both cases.

3. Numerical algorithm

3.1. *Discretization*

The computational mesh is unstructured and built with square cells of constant size h. Grid points are introduced dynamically during the computation in regions of non-negligible vorticity and are deleted where and when vorticity becomes negligibly small. The data structure, illustrated in figure 1, is organized in such a way that, for each row, a pointer to the first non-empty grid point (column) is stored and, for each grid point, a pointer to the nearest rightward cell is stored.

A distinction has to be drawn between an inner cell c that is completely encircled by four other cells and a cell belonging to one of the boundaries of the computational domain: no-slip wall, inflow, outflow and external artificial boundary. The last is defined by the cells bordering negligible vorticity regions (i.e. such that at least one of the four neighbouring cells is not present in the mesh); its presence is necessary in order to limit the theoretical unbounded domain.

The terms $\bar{\psi}$ and $\bar{\omega}$ are assumed known at time $\tau^{(n)}$ (n specifies the time iteration), whereas they are unknown and are computed by an implicit algorithm at time level

https://doi.org/10.1017/S0022112001007340 Published online by Cambridge University Press

$n+1$. The Poisson equation for the streamfunction is discretized by the usual second-order central difference operator at time $\tau^{(n+1)}$. In the vorticity-transport equation, the velocity components are computed from the streamfunction explicitly determined at time level $n+\frac{1}{2}$ by Adams extrapolation. The convective derivatives are discretized in conservation form. The obtained discretization is somewhat different from the usual totally explicit Adams time advancement; in fact, vorticity is implicit although stream function is explicit. In addition, an upwind bias is introduced in the implicit part of the vorticity equation in order to obtain a good conditioning of the implicit linear system without destroying second-order accuracy. Finally, the time derivative and the diffusion term are discretized by a classical Crank–Nicholson scheme. A detailed description of the adopted discretization can be found in Appendix A.

3.2. *Boundary conditions*

It is necessary to define a numerical condition on the finite outer boundary of the computational domain in order to close the problem for the Poisson equation in (2.6). For this purpose we obtained the numerical values of the streamfunction on the external boundary by using the Green function for the general unbounded domain around a semi-infinite wedge of angle β. The streamfunction is then obtained by a relation of the form

$$\bar{\psi}(\bar{x},\bar{y},\bar{t}\,) = \bar{t}\,\mathrm{Re}(\bar{z}^m) - \frac{1}{2\pi}\int_S \bar{\omega}(\bar{x}_0,\bar{y}_0,\bar{t}\,)G(\bar{z},\bar{z}_0)\mathrm{d}S_0, \tag{3.1}$$

where $\bar{z} = \bar{x} + I\bar{y}$ ($I = \sqrt{-1}$) and G is the Green function of the considered problem. Details on the derivation of this boundary condition are given in Appendix B with some useful modifications allowing for a reduction of the plate length in the computational domain. Equation (3.1), in principle, provides the streamfunction in the complete domain, but it is only used to compute $\bar{\psi}$ on the outer boundary (artificial, inflow, outflow), otherwise the computation of the Green integral in the complete domain would require impractically large computing times.

Following equation (2.2), on the plate, $\bar{\psi}$ is set to zero. Moreover, vorticity is related to the streamfunction in the inner flow by Thom's relation:

$$\bar{\omega}(\bar{x},0^+,\bar{t}\,) = \frac{2}{h^2}\bar{\psi}(\bar{x},+h,\bar{t}\,), \quad \bar{\omega}(\bar{x},0^-,\bar{t}\,) = \frac{2}{h^2}\bar{\psi}(\bar{x},-h,\bar{t}\,), \quad \bar{x}<0, \tag{3.2}$$

and a similar formula is applied at the edge of the plate:

$$\bar{\omega}(0,0,\bar{t}\,) = \frac{1}{h^2}[\bar{\psi}(0,-h,\bar{t}\,) + \bar{\psi}(+h,0,\bar{t}\,) + \bar{\psi}(0,+h,\bar{t}\,)]. \tag{3.3}$$

3.3. *Multigrid integration scheme*

The linear system obtained by discretizing the streamfunction and vorticity equations is simultaneously solved for the unknowns $\bar{\psi}_c^{(n+1)}$, $\bar{\omega}_c^{(n+1)}$ by a V-cycle, linear multigrid technique with one pre/post-smoothing as described, for instance, in Wesseling (1992 p. 173).

The smoothing algorithm is red-black point relaxation. This is very simple and its smoothing properties are as good as any other's for the present problem. In a classical full multigrid V-cycle the smoothing factor of red-black is of the order of 3, meaning that the error norm is reduced by a factor of approximately 3 for each complete cycle, but this factor can be increased to 9 with the modification proposed in Luchini & D'Alascio (1994), to which we refer for a description of the algorithm with application to the solution of the Poisson equation in a structured Cartesian

https://doi.org/10.1017/S0022112001007340 Published online by Cambridge University Press

mesh. The convergence speed improvement is essentially due to a modification of the restriction phase which takes into account the already available residual on the finer grid. This is equivalent to gaining an additional red-black smoothing at no cost.

In order to apply a multigrid to the present problem, the largest development effort required was for the management of the unstructured mesh, because of the continually changing shape of the computational domain.

The procedure adopted for creating each coarser grid from the next finer one consists of adding a coarse cell, specified by row and column indices (ic, jc), if and only if the corresponding fine grid cell, specified in the finer grid frame by indices (if, jf) = ($2ic$, $2jc$), is present. In this way, the coarse grid is always enclosed in the fine grid. Subsequently, a scan is done to identify the external artificial boundary of the coarse grid where artificial boundary conditions will be imposed. This procedure is recursively applied, up to the coarsest grid required.

The linear system to be solved for a given level is built in terms of the coarse grid corrections $\delta\bar{\psi}$ and $\delta\bar{\omega}$ for each inner grid cell following the discretization specified in equations (A 1)–(A 4) and has the following structure:

$$\left.\begin{aligned} &\delta\bar{\psi}_l + \delta\bar{\psi}_u - 4\delta\bar{\psi}_c + \delta\bar{\psi}_d + \delta\bar{\psi}_r - h^2\delta\bar{\omega}_c = \mathrm{rhs}_\psi, \\ &l_c\delta\bar{\omega}_l + u_c\delta\bar{\omega}_u + c_c\delta\bar{\omega}_c + d_c\delta\bar{\omega}_d + r_c\delta\bar{\omega}_r = \mathrm{rhs}_\omega. \end{aligned}\right\} \tag{3.4}$$

The right-hand side of the streamfunction equation is zero on the finest grid level.

The definition of the coefficients of the difference operators on each coarser mesh is trivial for the Poisson equation (they do not change), but some care is necessary in setting up the coefficients of the vorticity equation because they depend both on the mesh size and on the time step. For every grid level, the mesh size doubles while the time step remains unchanged, thus a re-computation of the coefficients of $\delta\bar{\omega}$ is required. In the case of a pure diffusion problem, it is possible to compute them efficiently in terms of their values at the fine grid level:

$$\left.\begin{aligned} &c_c^c = 4c_c^f + 3(l_c^f + r_c^f + d_c^f + u_c^f), \\ &l_c^c = l_c^f, \quad r_c^c = r_c^f, \quad d_c^c = d_c^f, \quad u_c^c = u_c^f, \end{aligned}\right\} \tag{3.5}$$

where sub/superscripts f and c specify, respectively, fine and coarse grid level.

These relations are also used with good results for the present advection–diffusion problem; the smoothing factor equal to 9, originally obtained for the solution of the Poisson equation, turns out to be thus preserved.

On the artificial boundary of the domain, at each coarser grid level, conditions of a Dirichlet type are specified as follows. If the coarse cell (ic, jc) corresponds to a fine cell (if, jf) belonging to the external boundary of the fine grid, the coarse grid corrections $\delta\bar{\psi}$ and $\delta\bar{\omega}$ are set to zero; in the opposite case, i.e. if the cell (if, jf) is internal in the fine grid level and a residual is available, $\delta\bar{\psi}$ and $\delta\bar{\omega}$ are computed by the modified restriction of Luchini & D'Alascio; these boundary conditions allow us to preserve the convergence properties of the original multigrid scheme.

The algorithm adopted in the multigrid 'V-cycle' can be summarized as follows:

(i) Smoothing of the solution on the current (fine) grid level.

(ii) Restriction to the coarser grid level with residual correction of Luchini & D'Alascio and computation of the coefficients of the linear system on the coarser level.

(iii) If another coarser mesh exists then recursive application of the present algorithm else solve the linear system.

https://doi.org/10.1017/S0022112001007340 Published online by Cambridge University Press

(iv) Prolongation of the solution to the finer grid level by linear interpolation of the coarser solution.

(v) Smoothing of the solution on the fine level.

The integration time is indeed very fast; the residual is reduced by almost 10 times in each cycle independently of the number of unknowns and mesh size.

After the computation of all variables at time $\tau^{(n+1)}$, an analysis of the flow at the external boundary allows us to rebuild the grid for the next time step. The local value of vorticity is compared with a given threshold; if it is higher, the former boundary cell is completely encircled with new cells with zero vorticity and the stream function obtained from the Green integral; if the value is lower than the threshold and this is also true for all existing neighbouring cells, the grid point is deleted.

3.4. *Local mesh refinement*

With time, the mesh size eventually becomes inadequate to resolve accurately the large flow gradients present near the edge of the plate. To preserve the accuracy of computation, a local mesh refinement has been introduced. This refinement was made possible by the multigrid technique.

A fixed number of square Cartesian submeshes centred in the edge of the plate has been added to the basic unstructured mesh of grid size h. If p refined grids are used, the resolution near the trailing edge is increased to a mesh size $h/2^p$. The size of each Cartesian submesh can be chosen freely, the only constraint being that it must be immersed in all the coarser grids.

At a given time step, the coefficients of the linear system to be solved are computed, for the basic grid and for all (the finer) subgrids, by applying the discretization described in Appendix A. Then a complete multigrid cycle is performed as described in the previous section taking care that the streamfunction and vorticity on the boundary of the subgrids, which are not available, are computed by cubic interpolation of the coarser values.

The multigrid technique with local mesh refinement effectively worked with convergence speed independent of the basic mesh size h with a smoothing factor of the order of 5, instead of 9 as in the basic algorithm.

4. Numerical results

Calculations were performed with different mesh sizes and exhibited, as will be shown, a substantial agreement. In all tests, the artificial conditions of inflow/outflow, required to bound the computational domain, were imposed at $\bar{x} \approx -50$. This distance was chosen so as to keep the reattachment point on the leeward side of the plate sufficiently far from the artificial boundary (the reattachment point position is $\bar{x} \approx -30$ at the end of each numerical simulation). On the finest tested mesh ($h = 0.1$), two Cartesian submeshes have been added near the edge of the plate:

(i) $h = 0.05$, 128×128 grid cells.

(ii) $h = 0.025$, 192×192 grid cells.

The tests were performed with about 1000 time steps and a number of cells in the basic grid (N) increasing from a few thousand at the beginning up to 100 000 at the end of the run.

In figure 2, the results obtained for $h = 0.1$ are presented. The solution at four different times is shown in the case of impulsive acceleration of the plate to a constant speed ($a = 0$). The iso-vorticity curves (iso-curve spacing $\Delta = 15$) show the evolution of the start-up vortex. As anticipated in § 1, the initial stage of the

https://doi.org/10.1017/S0022112001007340 Published online by Cambridge University Press

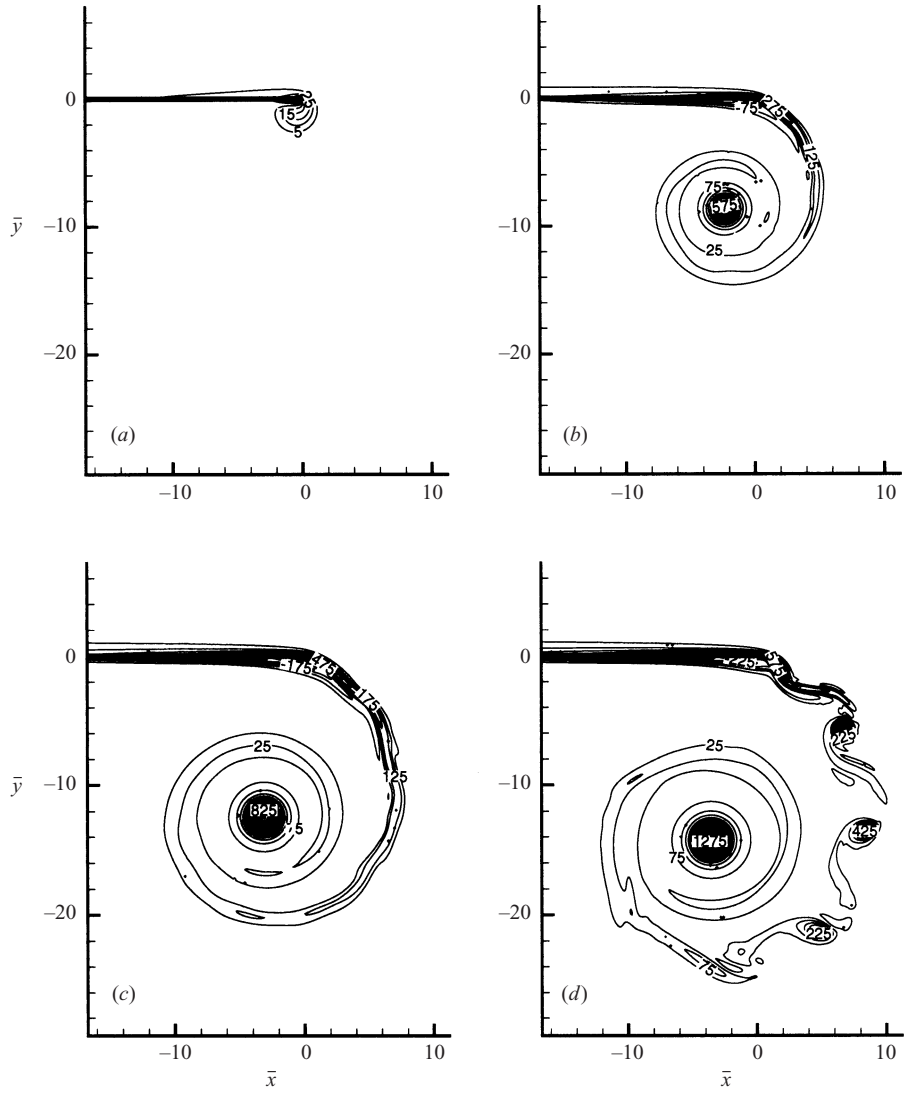


FIGURE 2. Solution at four different times of the impulsive start-up case ($a = 0$). Iso-curves of vorticity field $\bar{\omega}(\bar{x}, \bar{y}, \bar{t})$, ($\Delta = 15$). (*a*) $\bar{t} = 30.98$, $Re_S = 61.29$, $n = 280$, $N = 41\,317$; (*b*) $\bar{t} = 536.1$, $Re_S = 2743$, $n = 480$, $N = 54\,155$; (*c*) $\bar{t} = 906.0$, $Re_S = 5523$, $n = 620$, $N = 70\,314$; (*d*) $\bar{t} = 1164$, $Re_S = 7713$, $n = 1100$, $N = 83\,628$.

motion is characterized by the presence of a Rayleigh flow on the whole plate with a constant boundary-layer thickness; in figure 2(*a*), at $\bar{t} = 30.98$, the vorticity-layer thickness is still constant on most of the plate, but the vortex is just starting to form. At $\bar{t} = 536.1$, figure 2(*b*), the vortex has detached and a spiralling structure begins to appear while on the lower side of the plate a region of negative vorticity evolves, revealing the reverse boundary layer induced by the primary separation at the trailing edge. Perturbations become evident when two turns of the spiral are completed, $\bar{t} = 906.0$, figure 2(*c*). Subsequently, irregular motion dominates the flow even if a mean spiral vortex is still recognizable, figure 2(*d*), $\bar{t} = 1164$. The travelling lumps of vorticity clearly resemble the structures characterizing unstable vortex sheets.

https://doi.org/10.1017/S0022112001007340 Published online by Cambridge University Press

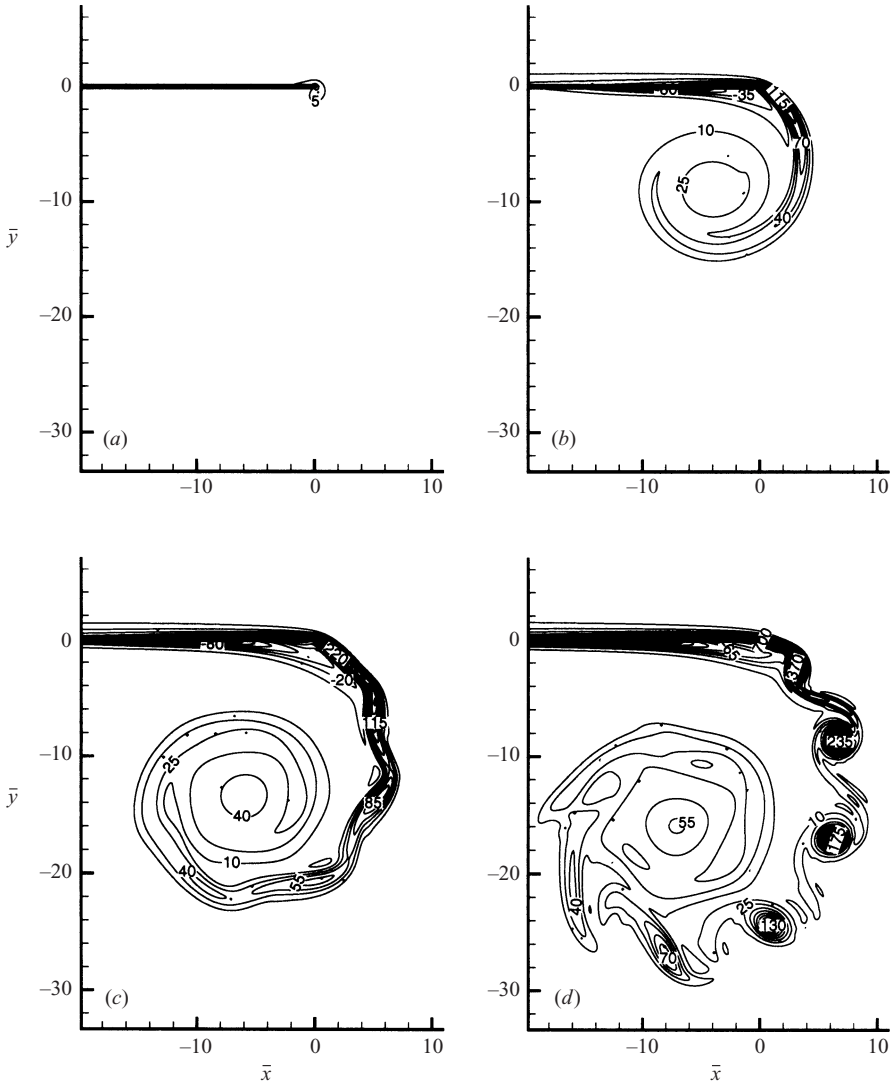


FIGURE 3. Solution at four different times of the constant acceleration start-up case ($a = 1$). Iso-curves of vorticity field $\bar{\omega}(\bar{x}, \bar{y}, \bar{t}\,)$, ($\Delta = 15$). (*a*) $\bar{t} = 13.89$, $Re_S = 35.97$, $n = 240$, $N = 58\,893$; (*b*) $\bar{t} = 304.5$, $Re_S = 2207$, $n = 420$, $N = 78\,769$; (*c*) $\bar{t} = 571.3$, $Re_S = 5106$, $n = 580$, $N = 107\,049$; (*d*) $\bar{t} = 738.8$, $Re_S = 7194$, $n = 740$, $N = 126\,916$.

Substantially similar results are obtained from the simulation of the constant acceleration case ($a = 1$), presented in figure 3. Once again, we observe the development of an irregular spiral vortex with a slight difference in core size and evolution of the spiral turns.

The characteristic time scale of the two presented simulations is completely different. For instance, by using the values of t_v derived in the examples of § 2, the times corresponding to the solutions displayed in figures 2(*d*) and 3(*d*) are ≈ 50 s and ≈ 0.3 s, respectively. However, it is very interesting to note that, in terms of the Pullin & Perry's Reynolds number Re_S, the instabilities become graphically visible in both tests for $Re_S = 4500 \sim 5000$.

https://doi.org/10.1017/S0022112001007340 Published online by Cambridge University Press

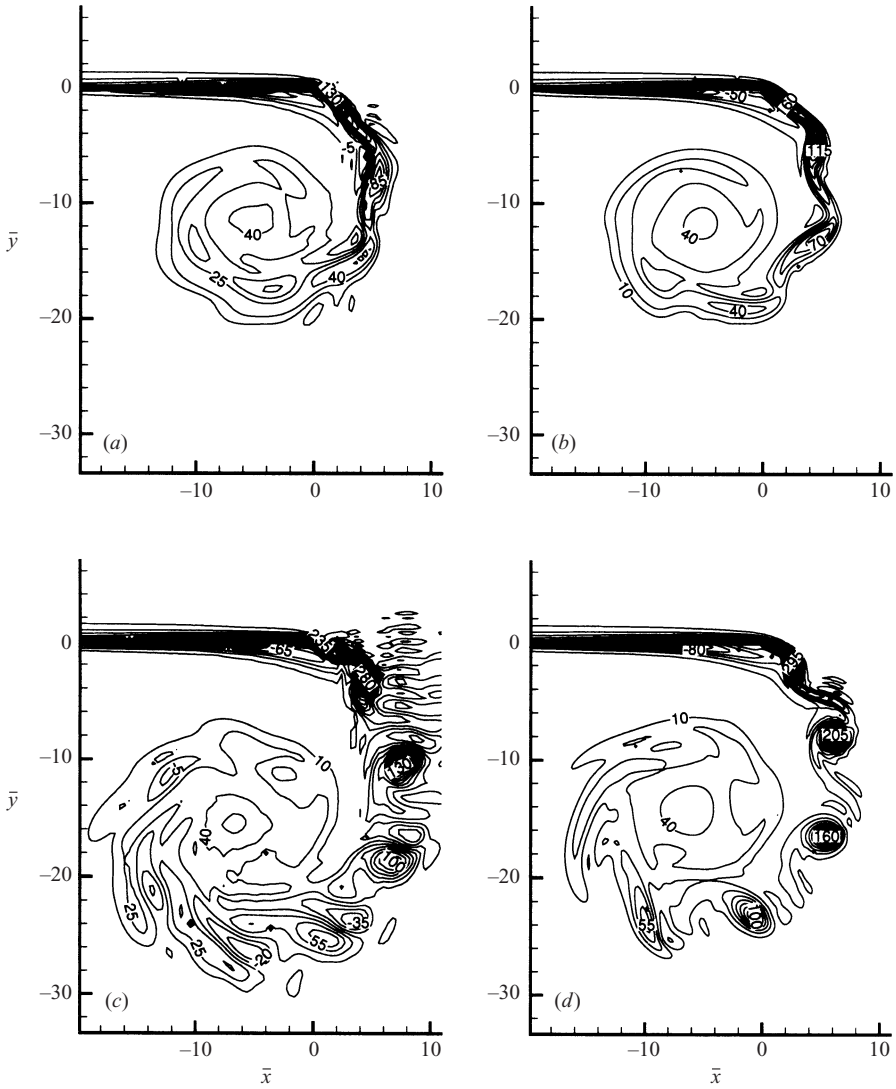


FIGURE 4. Case $a = 1$. Comparison between the simulation with basic grid size $h = 0.4$ and $h = 0.2$. Iso-curves of vorticity field $\bar{\omega}(\bar{x}, \bar{y}, \bar{t})$, ($\Delta = 15$). (*a*) $h = 0.4$, $\bar{t} = 472.5$, $Re_S = 3964$, $it = 180$, $N = 7128$; (*b*) $h = 0.2$, $\bar{t} = 476.3$, $Re_S = 4007$, $it = 280$, $N = 26\,241$; (*c*) $h = 0.4$, $\bar{t} = 730.7$, $Re_S = 7090$, $it = 400$, $N = 10\,107$; (*d*) $h = 0.2$, $\bar{t} = 636.5$, $Re_S = 5898$, $it = 540$, $N = 31\,036$.

We repeated the calculations by using three different mesh sizes for the basic grid ($h = 0.4$, $h = 0.2$ and the already presented case $h = 0.1$). In all tests, two submeshes were used for local refinement with the same dimensions in the $(\bar{x}, \bar{y})$-plane. In figure 4, the results for the case $a = 1$ ($h = 0.4$, $h = 0.2$) are presented. For the case $a = 0$, very similar results have been obtained and therefore are not reported.

With varying mesh size, the simulations showed a qualitative similar behaviour of the spiral evolution. The solutions on the coarser meshes are, however, characterized by the presence of numerical oscillations near the plate apex, which are clearly due to a local poor mesh resolution. Indeed, they disappear as the mesh size diminishes. In practice, near the plate apex we adopted a mesh size ranging from $h = 0.4$ to

https://doi.org/10.1017/S0022112001007340 Published online by Cambridge University Press

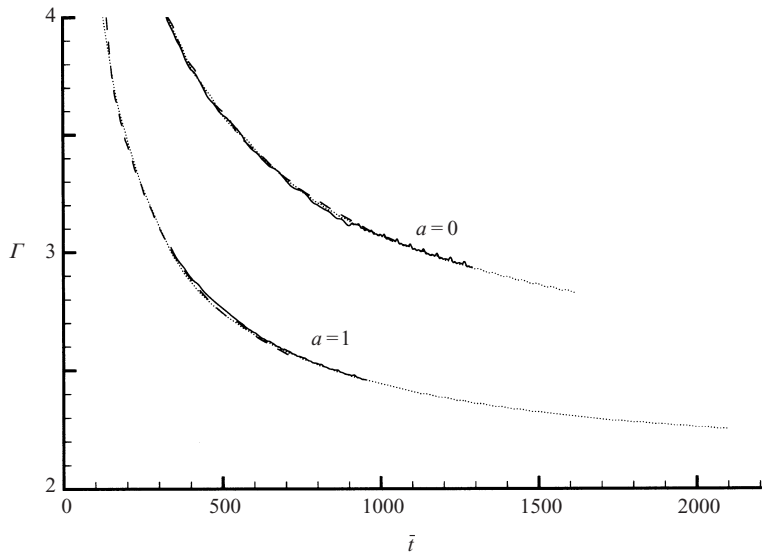


FIGURE 5. Total circulation Γ versus $\bar{t}$ computed with different meshes for cases $a = 0$ and $a = 1$. ——, $h = 0.4$; $\cdots$, $h = 0.2$; — — —, $h = 0.1$.

$h = 0.025$; that is, we increased the local grid resolution by a factor 16 and still obtained the same result. In all tests, the numerical experiments behaved like a turbulent flow with the formation of eddies along the still recognizable spiral sheet; therefore, a quantitative comparison among the tests performed with different meshes required the analysis of average quantities. It is interesting to perform this analysis in terms of the similarity variables of the inviscid spiral rolling-up (see, for instance, Saffman 1992 p. 152 for their determination). The inviscid similarity plane $\xi + I\eta = \zeta$ is related to $\bar{z}$ by the relation

$$\zeta = \left[\frac{(1+a)m^{(1-m)}}{k(2-m)}\right]^{1/(2-m)} \bar{t}^{-1/(2-m)}\bar{z}. \tag{4.1}$$

The total circulation in this plane is given by

$$\Gamma = \frac{2-m}{m(1+a)k} \iint \omega(\xi, \eta, T)\mathrm{d}\xi\, \mathrm{d}\eta. \tag{4.2}$$

The time histories of $\Gamma(\bar{t})$ are plotted in figure 5 for $a = 0$ and $a = 1$, as determined by the simulations with different mesh sizes. For large time values, $\Gamma(\bar{t})$ approaches an asymptotic value; differences among the simulations performed with different h are hardly visible. Similar results are obtained analysing the time histories of the vortex core coordinates ξ_c, η_c reported in figures 6 and 7, respectively, for the cases $a = 0$ and $a = 1$. The instantaneous position of the viscous vortex core has been computed by the relation:

$$\zeta_c(\bar{t}) = \frac{1}{\Gamma(\bar{t})} \frac{(2-m)}{m(1+a)k} \iint \omega(\xi, \eta, \bar{t})\zeta \mathrm{d}\xi\, \mathrm{d}\eta. \tag{4.3}$$

The plots again show an excellent agreement among the tests performed with different h with only a slight shift of η_c in the case $a = 0$. The vortex core position, in similarity variables, also tends to an asymptotic value. Furthermore, the figures evidence oscillations of very small amplitude which start when the instability appears.

https://doi.org/10.1017/S0022112001007340 Published online by Cambridge University Press

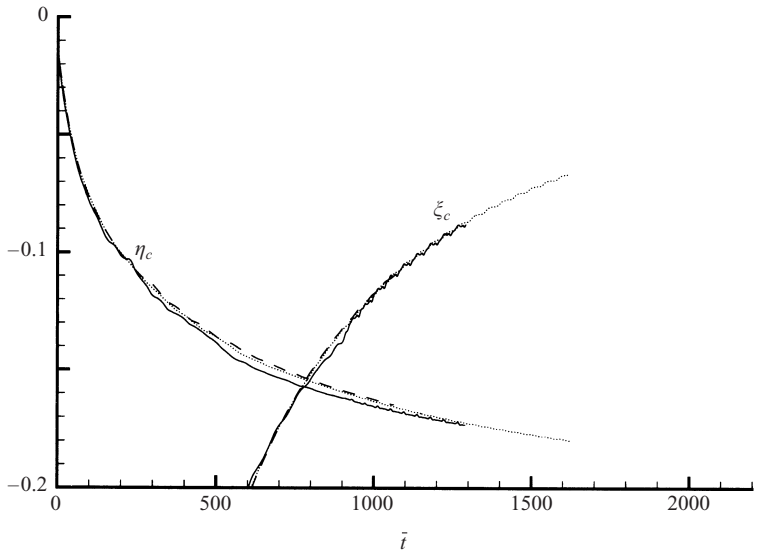


FIGURE 6. Vortex core coordinates ζ_c versus $\bar{t}$ computed with different meshes. Case $a = 0$. ——, $h = 0.4$; ···, $h = 0.2$; – – –, $h = 0.1$.

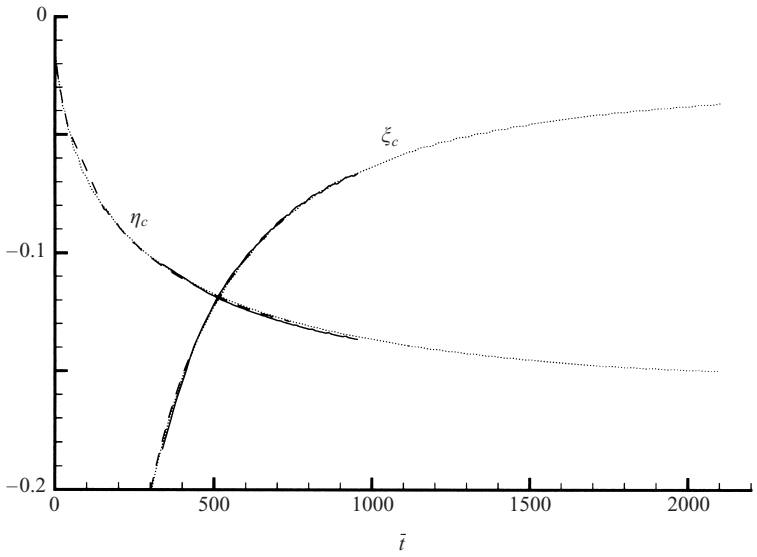


FIGURE 7. Vortex core coordinates ζ_c versus $\bar{t}$ computed with different meshes. Case $a = 1$. ——, $h = 0.4$; ···, $h = 0.2$; – – –, $h = 0.1$.

In tables 1 and 2, respectively, for the case $a = 0$ and $a = 1$, comparisons of the computed total circulation and vortex core position are presented for a specified time. They show that the maximum variations of Γ and ζ_c with mesh size are lower than 2%.

Particular care was also needed to handle the singularity at the edge of the plate. In fact, the edge is a source of small-scale perturbations even in the physical problem (as a singularity, it has an infinite wavenumber spectrum) and only viscosity sets the minimum length scale; therefore, in addition to adopting a local refinement of the

https://doi.org/10.1017/S0022112001007340 Published online by Cambridge University Press

	$h = 0.4$	$h = 0.2$	$h = 0.1$
Γ	3.074	3.066	3.072
ξ_c	−0.1178	−0.1185	−0.1174
η_c	−0.1655	−0.1634	−0.1625

TABLE 1. Γ and ζ_c obtained by simulations with different mesh size; case $a = 0$, $\bar{t} = 1000$.

	$h = 0.4$	$h = 0.2$	$h = 0.1$
Γ	2.586	2.579	2.570
ξ_c	−0.08737	−0.08826	−0.08820
η_c	−0.1286	−0.1273	−0.1277

TABLE 2. Γ and ζ_c obtained by simulations with different mesh size; case $a = 1$, $\bar{t} = 700$.

computational grid, we took great care to start the simulation from a small enough time (i.e. Reynolds number) that the stable viscous regime could be observed for a large number of steps before the instability showed up.

5. Comparison with the experiments

The present results can be usefully compared with Pierce's (1961) experimental results on the evolution of start-up spiral vortices around wedges of different shapes. Although a quantitative comparison is not possible owing to the different geometry, the shadowgraph images show streaklines of the flow which look impressively similar to the visualization of our numerical simulations. In both cases, the presence of localized spots of vorticity is accompanied by a growing complexity of the flow with time.

Pullin & Perry (1980) studied the same phenomenon by a different apparatus, in order to compare the experiments with the numerical inviscid self-similar solution of Pullin (1978). They could not completely verify the stability of the spiral vortex start-up since most of their results do not show regular and stable spirals. Having obtained a few pictures with a smooth spiral and a shape comparable to their numerical results, they conjectured the stability of the self-similar solution proposing apparatus vibrations as a possible source of the irregular experimental behaviour.

A different interpretation can be derived with the help of the present numerical simulations. The main difference between Pierce's and Pullin & Perry's experiments lies in their test Reynolds number. Whereas in the experiments of Pullin & Perry, Re_S was of the order of 1000, in the tests of Pierce, Re_S ranged in the interval $(10^4$–$10^5)$; this difference, noted but not highlighted in the original papers, has a large impact on the results, because, as observed in the previous section, in all of our tests, the instabilities revealed themselves for $Re_S \approx 5000$.

We numerically reproduced the experiment of Pullin & Perry that approximates better a flat plate flow ($a = 0.45$, $\beta = 5°$). The vorticity patterns are, as may be expected, intermediate between those corresponding to $a = 0$ and to $a = 1$. The corresponding experiment attained the highest Reynolds number among their performed tests: $Re_S = 4268$, $t = 5.68$ s, and reported the most irregular streaklines. In our numerical test with $a = 0.45$, the non-dimensional time at which unstable behaviour starts to become visible is $\bar{t} = 600$, equivalent to $Re_S = 4500$ and $t = 6.9$ s: the numerical results are even smoother than the experimental ones. Nonetheless, the

https://doi.org/10.1017/S0022112001007340 Published online by Cambridge University Press

relatively smooth results of the experiment can be ascribed to the fact that it was stopped too early.

Unfortunately, we cannot reproduce the most regular test of Pullin & Perry because it is too far from a flat plate configuration ($\beta = 60^\circ$, $a = 0$). We have to remark, however, that this experiment was performed with an even lower maximum Re_S (1117). As far as a qualitative comparison with $a = 0$ and $\beta = 0^\circ$ is significant, we can observe that our data do provide a regular spiral for the time corresponding to the experiment. In fact, the actual duration of the experiments ($t = 10$ s, equivalent to $Re_S = 1000$ for the flat plate with step-velocity start-up) corresponds to $\bar{t} = 260$ in the numerical simulation displayed in figure 2 which is a time in which viscous effects are still comparable with convective ones. In figure 2(*d*), the flow is dominated by vorticity spots for $Re_S \approx 7700$; this value would be far beyond the range obtainable by Pullin & Perry's experimental apparatus.

As a final remark, small oscillations with time of the vortex-core position (similar to those presented in figures 6 and 7) were also reported by Pullin & Perry. Furthermore, our simulations do not yet reveal any formation of a secondary spiral vortex with opposed sign circulation at their final time. This is in agreement with Pullin & Perry's results that show the birth of a secondary vortex only for the larger values of the wedge angle β.

In the already cited work of Koumoutsakos & Shiels (1996), a viscous simulation of the start-up of a plate of finite thickness was performed by a blob method. While their conclusions are in agreement with the present ones for the case $a = 1$, i.e. they also observe the formation of irregular vorticity spots, for the impulsive case ($a = 0$), Koumoutsakos & Shiels obtained a regular vortex spiral evolution. However, a comparison of the results requires some caution. The simulation of a semi-infinite plate gave us the possibility of concentrating on the simulation of the self-similar stage of the spiral-vortex evolution, while Koumoutsakos & Shiels also included the vortex-expulsion phase.

In their results, the self-similar evolution of the spiral vortex could barely be seen in the tests with the largest Reynolds numbers, and then only for a very short time before the vortices were convected downstream. By casting their results in our time units, it can be reckoned that the self-similar stages ended at $\bar{t} \approx 200$ in both their impulsive and uniform-acceleration tests corresponding to $Re_S \approx 700$ ($a = 0$) and $Re_S \approx 1300$ ($a = 1$). As previously noted, our calculations show the appearance of irregularities for $Re_S > 4500$ in both tests. Hence, oscillations in the spiral should not have appeared at all in either case. However, the threshold at which oscillations become visible clearly depends on the amount of numerical noise present in the simulation; the fact that Koumoutsakos & Shiels were forced to adopt a lower resolution in order to model a more complex geometry may explain why they did see something in the case that, during the self-similar stage, reached the largest Reynolds number.

Wang *et al.* (1999) confirmed the instability of the vortex spiral for the impulsive start-up in the case of flow around an ellipse, highlighting the remarkable qualitative agreement with Pierce's experimental results.

6. Conclusions

A numerical method has been presented for the two-dimensional simulation of the start-up vortex issuing from a semi-infinite flat plate accelerated from rest in still air. The algorithm solves the $\psi - \omega$ formulation of the incompressible Navier–Stokes equations. Particular care has been devoted to the development of an efficient numer-

https://doi.org/10.1017/S0022112001007340 Published online by Cambridge University Press

ical scheme. The number of grid cells is minimized by using a non-dimensionalization of the flow equations based on the Rayleigh layer thickness and a varying time step; in these coordinates an unstructured grid with square cells is dynamically defined at each time step so that computations are only performed in regions of non-negligible vorticity. An implicit discretization with a fast simultaneous integration of the stream-function and vorticity equations has been obtained by use of a multigrid technique with a smoothing factor of 9. Moreover, the efficiency of the algorithm has been further improved by implementing a local mesh refinement near the plate edge within the context of the multigrid strategy. The CPU time bottle-neck of the simulations was given by the time required for the calculation of the Green integral in the external boundary cells, which has a non-linear growth versus the number of grid points while the internal integration is still very fast (linear). There is, therefore, still room for improvement.

The results for two time laws of acceleration have been displayed: uniform and impulsive acceleration of the plate. In both cases, the viscous solution starts to exhibit oscillations as soon as a recognizable vortex spiral is formed. The evolution of the oscillations bears some resemblance to the Kelvin–Helmholtz instability of a plane vortex sheet. In all the performed calculations, the instability appeared for $Re_S \approx 4500$. These results have been confirmed by repeating the computations with different mesh sizes, the time histories of integral parameters, as the total circulation or the vortex core position, are in excellent agreement.

These results provide insight into a phenomenon which is still debated and not completely clarified by experimental evidence. The qualitative agreement of the numerical simulations with the results of Pierce's experiments is noteworthy. On the other side, our calculations suggest that Pullin & Perry's experimental results are not necessarily in disagreement with Pierce's: the discrepancies are due to a difference in Reynolds number (or equivalently in time scale). In Pullin & Perry's tests, the vortex spirals are in an earlier stage in which viscous effects are comparable with the convective ones ($Re_S \ll 4500$) whereas Pierce's results show a later stage in which an unstable inviscid flow has developed.

Appendix A. Numerical discretization of the Navier–Stokes equations

The discretization of the Poisson equation for the streamfunction at time $\tau^{(n+1)}$ is obtained by standard central differencing (subscripts are defined in figure 1):

$$\bar{\psi}_l^{(n+1)} + \bar{\psi}_u^{(n+1)} - 4\bar{\psi}_c^{(n+1)} + \bar{\psi}_d^{(n+1)} + \bar{\psi}_r^{(n+1)} = h^2 \bar{\omega}_c^{(n+1)}. \tag{A 1}$$

In the vorticity-transport equation the velocity at time $\tau^{(n+1/2)}$ is computed by Adams extrapolation:

$$\left.\begin{aligned} \bar{\psi}_{i,j}^{(n+1/2)} &= \bar{\psi}_{i,j}^{(n)} + \frac{\Delta\tau}{2\Delta\tau_{old}}[\bar{\psi}_{i,j}^{(n)} - \bar{\psi}_{i,j}^{(n-1)}], \\ u_{i,j} &= \frac{1}{2h}[\bar{\psi}_{i,j+1}^{(n+1/2)} - \bar{\psi}_{i,j-1}^{(n+1/2)}] - \tfrac{1}{2}kjh, \\ v_{i,j} &= -\frac{1}{2h}[\bar{\psi}_{i+1,j}^{(n+1/2)} - \bar{\psi}_{i-1,j}^{(n+1/2)}] - \tfrac{1}{2}kih, \end{aligned}\right\} \tag{A 2}$$

with $\Delta\tau = [\tau^{(n+1)} - \tau^{(n)}]$ and $\Delta\tau_{old} = [\tau^{(n)} - \tau^{(n-1)}]$.

The convective derivatives are discretized in conservation form. For the $\bar{x}$-direction

https://doi.org/10.1017/S0022112001007340 Published online by Cambridge University Press

term (in the $\bar{y}$-direction the discretization is similar):

$$\left.\begin{aligned}
&u^{(-)} = \tfrac{1}{2}(u_{i,j-1} + u_{i,j}) = \tfrac{1}{2}(u_l + u_c),\\
&u^{(+)} = \tfrac{1}{2}(u_{i,j} + u_{i,j+1}) = \tfrac{1}{2}(u_c + u_r),\\
&u_c \geqslant 0: \quad \frac{\partial}{\partial \bar{x}}(u\bar{\omega})_c^{(n+1/2)} = \frac{1}{2}\left[\frac{1}{h}\left(u^{(+)}\bar{\omega}_r^{(n)} - u^{(-)}\bar{\omega}_c^{(n)}\right)\right.\\
&\qquad\qquad\qquad\qquad \left. + \frac{1}{h}\left(u^{(+)}\bar{\omega}_c^{(n+1)} - u^{(-)}\bar{\omega}_l^{(n+1)}\right)\right],\\
&u_c < 0: \quad \frac{\partial}{\partial \bar{x}}(u\bar{\omega})_c^{(n+1/2)} = \frac{1}{2}\left[\frac{1}{h}\left(u^{(+)}\bar{\omega}_r^{(n+1)} - u^{(-)}\bar{\omega}_c^{(n+1)}\right)\right.\\
&\qquad\qquad\qquad\qquad \left. + \frac{1}{h}\left(u^{(+)}\bar{\omega}_c^{(n)} - u^{(-)}\bar{\omega}_l^{(n)}\right)\right].
\end{aligned}\right\} \tag{A 3}$$

The difference formulae of the time derivative and of the diffusion of vorticity are obtained by the Crank–Nicholson scheme:

$$\left.\begin{aligned}
\left(\frac{\partial}{\partial \tau}\bar{\omega}\right)_c^{(n+1/2)} &= \frac{1}{\Delta\tau}\left[\bar{\omega}_c^{(n+1)} - \bar{\omega}_c^{(n)}\right],\\
(\bar{\nabla}^2\bar{\omega})_c^{(n+1/2)} &= \frac{1}{2h^2}\left\{\left[\bar{\omega}_l^{(n)} + \bar{\omega}_u^{(n)} - 4\bar{\omega}_c^{(n)} + \bar{\omega}_d^{(n)} + \bar{\omega}_r^{(n)}\right]\right.\\
&\quad \left. + \left[\bar{\omega}_l^{(n+1)} + \bar{\omega}_u^{(n+1)} - 4\bar{\omega}_c^{(n+1)} + \bar{\omega}_d^{(n+1)} + \bar{\omega}_r^{(n+1)}\right]\right\}.
\end{aligned}\right\} \tag{A 4}$$

The time step $\Delta\tau$ is recomputed at each time iteration and is chosen by constraining the maximum variation of vorticity in a time step to a predefined value. For instance in our calculations we adopted the constraint

$$\Delta = \frac{|\bar{\omega}_c^{(n)} - \bar{\omega}_c^{(n-1)}|_{max}}{|\bar{\omega}_c^{(n)}|_{max}} \approx 0.1, \tag{A 5}$$

which was satisfied by setting at each time iteration

$$\Delta\tau = \Delta\tau_{old}\left(\frac{0.1}{\Delta}\right)^{0.3}. \tag{A 6}$$

Appendix B. Boundary condition on the external boundary

We split the streamfunction into two contribution, $\bar{\psi} = \bar{\psi}_1 + \bar{\psi}_2$.

$\bar{\psi}_1$ is computed by solving the Laplace equation with the actual boundary conditions:

$$\left.\begin{aligned}
&\bar{\nabla}^2\bar{\psi}_1 = 0,\\
&\bar{\psi}_1(\bar{x}, 0^{\pm}, \bar{t}) = 0, \quad \bar{x} < 0,\\
&\bar{r} \to \infty : \bar{\psi}_1 \to \bar{\psi}_\infty(\bar{r}, \bar{\theta}, \bar{t}).
\end{aligned}\right\} \tag{B 1}$$

$\bar{\psi}_2$ can be determined by solving the Poisson equation with homogeneous boundary conditions:

$$\left.\begin{aligned}
&\bar{\nabla}^2\bar{\psi}_2 = \bar{\omega},\\
&\bar{\psi}_2(\bar{x}, 0^{\pm}, \bar{t}) = 0, \quad \bar{x} < 0,\\
&\bar{r} \to \infty : \bar{\psi}_2 \to 0.
\end{aligned}\right\} \tag{B 2}$$

https://doi.org/10.1017/S0022112001007340 Published online by Cambridge University Press

The solution of (B 1) is

$$\bar{\psi}(\bar{x},\bar{y},\bar{t}\,) = \bar{t}\,\mathrm{Re}(\bar{z}^m), \tag{B 3}$$

with $\bar{z} = \bar{x} + \mathrm{i}\bar{y}$ ($\mathrm{i} = \sqrt{-1}$).

The homogeneous problem (B 2) can be solved by using the Green function for the general unbounded domain around a semi-infinite wedge of angle β:

$$G(\bar{z},\bar{z}_0) = -\ln\left(\left|\frac{\bar{z}^m - \bar{z}_0{}^m}{\bar{z}^m - (\bar{z}_0{}^m)^*}\right|\right), \tag{B 4}$$

obtaining

$$\bar{\psi}_2(\bar{x},\bar{y},\bar{t}\,) = -\frac{1}{2\pi}\int_S \bar{\omega}(\bar{x}_0,\bar{y}_0,\bar{t}\,)G(\bar{z},\bar{z}_0)\mathrm{d}S_0. \tag{B 5}$$

Suitable boundary conditions have been introduced at inflow and outflow in order to account for the finite length of the plate included in the computational domain. At outflow the condition $\bar{\omega}_{\bar{x}} = 0$ is used, which is consistent with Rayleigh-type flow, the asymptotic behaviour of the solution at both inflow and outflow. In a first attempt, we applied the same condition at the inflow boundary but obtained clearly unacceptable solutions. In fact, a recirculation bubble formed just aft of the inflow boundary instead of the asymptotic behaviour of Rayleigh-type flow. This problem disappeared when we improved the numerical implementation of equation (B 5). In fact, the numerical computation of the integral in (B 5) can be done in the finite computational domain only. In this way the contribution of the semi-infinite vortical layers near the plate in the region external to the inflow/outflow is not considered. To take into account this contribution, we looked for an approximated analytical computation of the neglected boundary layer matching at the inflow, for each time step, the computed layer.

In the case of flat plate ($\beta = 0$, $m = \frac{1}{2}$), let us consider the conformal mapping $\bar{Z} = \bar{X} + \mathrm{i}\bar{Y} = \bar{z}^{1/2}$ of the physical domain into the half-plane. The field associated to the streamfunction:

$$\bar{\psi}_f = -C(1 - \mathrm{e}^{-\bar{X}/\delta}) \tag{B 6}$$

is characterized by the vorticity distribution

$$\bar{\omega}_f = \left|\frac{\mathrm{d}\bar{Z}}{\mathrm{d}\bar{z}}\right|^2 \frac{\partial^2}{\partial \bar{X}^2}\bar{\psi}_f = \frac{C}{4(\bar{X}^2 + \bar{Y}^2)\delta^2}\mathrm{e}^{-\bar{X}/\delta}, \tag{B 7}$$

$\bar{\psi}_f$ and $\bar{\omega}_f$ approximate a boundary-layer-like flow and provide the values of the constants C and δ. These coefficients can be computed by imposing the matching (on an integral basis) of the vorticity distribution with the numerical solution at the inlet ($\bar{x} = \bar{x}_{in}$, $\bar{y} > 0$):

$$\left.\begin{aligned}\int_0^\infty \bar{\omega}_f(\bar{x}_{in},\bar{y},\bar{t}\,)\mathrm{d}\bar{y} &= \int_0^\infty \bar{\omega}(\bar{x}_{in},\bar{y},\bar{t}\,)\mathrm{d}\bar{y},\\ \int_0^\infty \bar{\omega}_f(\bar{x}_{in},\bar{y},\bar{t}\,)\bar{y}\,\mathrm{d}\bar{y} &= \int_0^\infty \bar{\omega}(\bar{x}_{in},\bar{y},\bar{t}\,)\bar{y}\,\mathrm{d}\bar{y}.\end{aligned}\right\} \tag{B 8}$$

Hence, equation (B 5) can be approximated as

$$\bar{\psi}_2(\bar{x},\bar{y},\bar{t}\,) \approx \bar{\psi}_f - \frac{1}{2\pi}\int_{S_n}[\bar{\omega}(\bar{x}_0,\bar{y}_0,\bar{t}\,)G(\bar{z},\bar{z}_0) - \bar{\omega}_f(\bar{x}_0,\bar{y}_0,\bar{t}\,)G(\bar{z},\bar{z}_0)]\mathrm{d}S_0, \tag{B 9}$$

with S_n the bounded computational domain.

https://doi.org/10.1017/S0022112001007340 Published online by Cambridge University Press

Finally, the adopted formula for the computation of the streamfunction on the outer boundary is:

$$\bar{\psi}(\bar{x},\bar{y},\bar{t}\,) = \bar{t}\mathrm{Re}(\bar{z}^m) + \bar{\psi}_f - \frac{1}{2\pi}\int_{S_n}[\bar{\omega}(\bar{x}_0,\bar{y}_0,\bar{t}\,) - \bar{\omega}_f(\bar{x}_0,\bar{y}_0,\bar{t}\,)]G(\bar{z},\bar{z}_0)\mathrm{d}S_0. \qquad \text{(B 10)}$$

With this improvement, the recirculation bubble next to the inflow disappeared; the simulation of the vortex appears to be correct until the reattachment point on the leeward side of the plate approaches the outflow boundary.

REFERENCES

Batchelor, G. K. 1967 *An Introduction to Fluid Dynamics*. Cambridge University Press.

Koumoutsakos, P. & Shiels, D. 1996 Simulations of the viscous flow normal to an impulsively started and uniformly accelerated flat plate. *J. Fluid Mech.* **328**, 177–227.

Krasny, R. 1991 *Vortex Sheet Computations: Roll-up, Wakes, Separation.* Lecture Notes in Applied Mathematics, vol. 28, pp. 385–401. Springer.

Luchini, P. & D'Alascio, A. 1994 Multigrid pressure correction techniques for the computation of quasi-incompressible internal flows. *J. Numer. Meth. Fluids* **18**, 489–507.

Luchini, P. & Tognaccini, R. 1999 Comparison of viscous and inviscid numerical simulations of the start-up vortex issuing from a semi-infinite plate. *Conf. Proc. of Third International Workshop on Vortex Flows and Related Numerical Methods http://www.emath.fr/proc/Vol.7/*, pp. 247–257.

Moore, D. W. 1976 The stability of an evolving two-dimensional vortex sheet. *Mathematika* **23**, 35–44.

Pierce, D. 1961 Photographic evidence of the formation and growth of vorticity behind plates accelerated from rest in still air. *J. Fluid. Mech.* **11**, 460–464.

Pullin, D. I. 1978 The large-scale structure of unsteady self-similar rolled-up vortex sheets. *J. Fluid. Mech.* **88**, 401–430.

Pullin, D. I. & Perry, A. E. 1980 Some flow visualization experiments on the starting vortex. *J. Fluid. Mech.* **97**, 239–255.

Rott, N. 1956 Diffraction of a weak shock with vortex generation. *J. Fluid. Mech.* **28**, 111–128.

Saffman, P. G. 1992 *Vortex Dynamics*. Cambridge University Press.

Sarpkaya, T. 1989 Computational methods with vortices – The 1988 Freeman Scholar Lecture. *J. Fluids Engng* **111**, 5–52.

Wang, Z. J., Liu, J. G. & Childress, S. 1999 Connection between corner vortices and shear layer instability in flow past an ellipse. *Phys. Fluids* **11**, 2446–2448.

Wesseling, P. 1992 *An Introduction to Multigrid Methods*. John Wiley, Chichester.

https://doi.org/10.1017/S0022112001007340 Published online by Cambridge University Press